Photocatalytic Degradation of Bisphenol A Induced by Dense Nanocavities Inside Aligned 2D-TiO2 Nanostructures

Photocatalytic Degradation of Bisphenol A Induced by Dense Nanocavities Inside Aligned 2D-TiO_2 Nanostructures

Snejana Bakardjieva[a], Radek Fajgar[b], Ivo Jakubec[a], Eva Koci[a], Alexander Zhigunov[c], Efthalia Chatzisymeon[d], Konstantina Davididou[d]

[a]*Institute of Inorganic Chemistry of the CAS, 250 68 Husinec – Řež 1001, Czech Republic*

[b]*Institute of Chemical Process and Fundamentals of the CAS, Rozvojova 2/135, 165 02 Prague, CR*

[c]*Institute of Macromolecular Chemistry of the CAS, Heyrovskeho nam.1888/2, 162 00 Prague, Czech Republic*

[d] *School of Engineering, Institute for Infrastructure and Environment, The University of Edinburgh, Edinburgh EH9 3JL, United Kingdom*

Corresponding author Snejana Bakardjieva (email: snejana@iic.cas.cz)

Abstract

The preparation of materials with aligned porosity in the nanometer range is of technological importance for a wide range of applications in molecular filtration, biomaterials and catalysis. Herein we present the advantages offered by cryo – lyophilisation technique as a smart and green non-standard concept to produce dense regular polyhedral nanocavities inside the 2D TiO_2 nanosheets. Hierarchical morphologies of nanocavities start to appear at temperature higher than 800 °C and are strongly influenced by polymorph TiO_2 evolution competing reactions. The small angle X-ray scattering (SAXS) analysis confirms self-assembled 3D nanocavities with size range from 5 to 10 nm in both length and width, and depth ~ 3.6 nm formed after realising of the confined ice-water. It was found that nanocavities enhance significantly the absorption properties of TiO_2 in the UV region, thereby providing a new approach to increase the photoreactivity of 2D TiO_2 nanosheets. The annealed precursors containing aqueous solution of peroxo polytitanic acid (PPTA) at 800 °C exhibited the highest photoactivity in degrading bisphenol A (BPA) due to evenly distributed nanocavities inside single anatase TiO_2 nanocrystals interconnected and aligned onto the 2D TiO_2 nanosheet arrays.

Keywords: freeze-drying; anatase TiO_2; nanoconfined water; nanocavities; photocatalysis; emerging pollutants

1. Introduction

Nanochemistry aims to extend the traditional length scales of synthetic chemistry and exploit the collective properties of organized assemblies. Structurally organized inorganic materials are important for emerging applications (e.g., sensing, catalysis, energy storage applications [1], molecular filtration, smart fillers and biotechnologies [2]), since they can offer a desirable combination of an extensive internal reactive surface along narrow nanopores with facile molecular transport through broad *"highways"* leading to and from these pores [3]. Among various nanostructured metal oxides, 2D nanosheets of layered titanium oxide are fairly unique in terms of subnanometer-level thickness, wide 2D surface, and high flexibility [4,5]. Theoretical calculations predict a significant enhancement of the optical absorbance in a thin silicon film with nanocavities indicating another route to increase the photoreactivity of semiconductors [6,7]. A cavity is defined as an internal space, large enough to accommodate the van der Waals sphere of a small atom or water (i.e., 0 = 1.4 Å) without being connected to the outside. Nanocavities are known as isolated nanospaces inside a solid [8-12]; these can be formed via different processes, such as bombardment, irradiation or by using different templates allowing for the achievement of bimodal and even trimodal pore-structured materials [13]. Template removal either by thermal or dissolution treatment yields a hierarchically organized material with a structure that is a replica of that of the original template. However, the achievement of hierarchical hybrid materials is still rare despite the widespread use of these processes. Thus, there is currently a continuing need for novel fabrication methodologies, as well as, for materials with increased levels of spatial organization and functionalities [14]. Recently, semiconductor-based photocatalytic materials have attracted attention for cleaning up toxic pollutants, of which TiO_2 has been found to be a most widely studied in heterogeneous catalysis [15] due to its high resistance to photocorrosion, low-cost, abundance, photocatalytic stability and chemical and biological inertness [16-18]. However, a few drawbacks of TiO_2 including a large band gap than 3 eV (~3.0 at 410 nm for rutile and ~3.2 at 285 nm for anatase), low electron mobility (1 $cm^2/V/s$), and short hole diffusion length (10–100 nm) limit its quantum efficiency [19, 20]. Various strategies have been investigated to attack these problems. For instance, one-dimensional (1D) TiO_2 nanostructures (nanorods, nanotubes, nanoribbons and nanowires) can provide a short diffusion length perpendicular to the charge collecting substrate, yielding a low recombination of electron–hole pairs.[21, 22].

Novel nanostructures with dence stacked nanocavities inside 1D morphology of TiO_2 have been prepared, which present excellent photocatalytic and electrochemical properties. Fu et

al. recognized that the photocatalytic activity of 1D-bicrystalline nanoribbons with alternate structure of TiO_2(B) and anatase under visible light irradiation was due to the formation of nanocavities inside the nanocrystals. Their research revealed that TiO_2(B) with nanocavities exhibited a narrow band gap and improved its absorbance coefficient in the UV region [23]. An enhanced optical absorption induced by dence nanocavities inside titania nanorods was also observed by Han et al [24]. The molar absorption coefficient of TiO_2 nanorods with nanocavities (when the incident light wavelength was below 385 nm and closed to 3.2 eV of the band gap of anatase TiO_2) was found to be about 25% higher than that of TiO_2 without nanocavities. An easy method on the synthesis of nanovoid-structured TiO_2 microcrystals via a sol-gel route using titanium isopropoxide as precursor was published by Usseglio et al.[25]. Their combined IR, Raman, and TEM study indicates that the nanovoids were formed during the thermal treatment in air at 773 K by the partial oxidation products (hydrogen carbonates, adsorbed carbon dioxide, and residual OR groups) of the organic part of the precursor. The nanovoid-structured TiO_2 microcrystals were active in the photodegradation of methylene blue, but with a much lower efficiency compared with the standard P25 TiO_2 commercial photocatalyst due to its significantly lower surface area.

Compared with 1D system, 2D TiO_2 materials demonstrate unique characteristics for applications in photocatalysis. Their benefit resulting from the the larger surface area promotes charge migration across the 2D TiO_2 laeyrs. In case that hollow patterns are involved in the surface of TiO_2 layers, the propagation properties of the light could be effectively controled by using decoupling of the directions of light absorption and increased photon–matter interaction via multiple reflection and scattering at the „cavity domains“. Additionally, hierarchical and branched nanostructures simultaneously provide the advantages of a rapid charge transfer pathway for carrier collection and possess a large surface area for increased reaction sites, as well as an excellent light trapping [26, 27].

Xing et al. reported fabrication of lightweight porous crystalline TiO_2 ceramics as a floating photocatalyst by a camphene-based freeze-drying route for pesticide micropolluted water degradation [28]. It was demostated that dimethoate, lindane, dipterex, malathion, and bentazone could be degraded effectively using the mesoporous TiO_2 materials without any oxygenation or stirring.

Up to now, little efforts have been concentrated on the growth of pre-lyophilized 2D TiO_2 nanostructures (nanosheets), which might arise from the narrowed using of freeze-drying technique in nanomaterials science Therefore, it is highly desirable to investigate the synthesis, properties and applications of 2D TiO_2 nanosheets with dense 3D nanocavities inside converted from lyophilized Ti containing precursors. The lyophilisation, or else freeze-drying, is a process that removes the solvent (typically water) from a material. The procedure is carried out using a simple principle of physics sublimation, known as the transition of a

substance from the solid to the vapor state, performed at low temperature and pressure by applying vacuum. The history of freeze-drying goes back to the ancient Incas, who preserved their foodstuff by freezing it in the mountains in winter time - the frozen water is removed through the low vapor pressure of the water in the surrounding air at high altitudes. Actually, lyophilisation was first developed actively during World War II due to transport of serum. After the war period, the Atlas GEA Niro Inc. pioneered in freeze-drying business and in 1961 builds a freeze-drying cabinet for Nestle group in Germany and Holland for the preservation of coffee and foodstuffs. Nowadays, lyophilization is well established in many industries and applied to various products and specimens, including pharmaceuticals, vaccines, diagnostics, biological materials, body tissue, foodstuffs, and even whole organisms. Despite its wide and increasing usage, many (nano)materials laboratories, especially these focusing on biopharmaceuticals,still think of freeze-drying as a complicated and sophisticated technology. A few years ago, our group reported improved properties of TiO_2 photocatalysts obtained by cryo-lyophilisation technique, but no attention was paid on the nanocavity phenomena [29]. Herein, we use cryo-lyophilization methodology as a novel and original non-standard green concept for the synthesis of ultrafine precursors containing aqueous colloids of peroxo-polytitanic $Ti^{(IV)}$ acid (PPTA). The high temperature treatment of lyophilized PPTA led to evolution of well-defined 2D-anatase TiO_2 nanosheets with dense regular polyhedral nanocavities (we used terminology "*nanopockets*" also) inside. We found that as-created dense nanocavities enhanced significantly the optical absorption properties of TiO_2 in the UV region, thereby providing a new approach to increase the photoreactivity of TiO_2 nanosheets for use in the photocatalytic degradation of Bisphenol A (BPA). BPA with IUPAC name 4,4'-(propane-2,2-diyl)diphenol, $(CH_3)_2C(C_6H_4OH)_2$is an organic xenobiotic that is used extensively in the synthesis of polycarbonate polymers and epoxy resins, with a global consumption over 5.5 million metric tonnes [30]. BPA has received considerable attention recently due to its endocrine-disrupting nature, environmental persistence and widespread detection in the water cycle [31]. Its exposure has been connected with growth, developmental and reproductive effects on aquatic invertebrates, fishes, amphibians, reptiles, birds and mammalian wildlife [32]. The effluent discharges from municipal wastewater treatment plants (WWTPs) is the main pathway of BPA in the aquatic environment [33, 34], a fact that highlights the need to upgrade the conventional WWTPs with treatment methods efficient in degrading bio-recalcitrant compounds, such as BPA. Here we adopted the "*anti-crystal growth*" model, proposed by Han et al. [24], as well as a structural topotaxy between the hydrogen titanate precursor and titania (anatase TiO_2) [35] in order to explain the plausible formation mechanism of nanocavities. The chemical and morphological characteristics of the 2D TiO_2 photocatalysts were studied by XRD and electron microscopy (SEM/EDS, HRTEM/SAED). X-ray photoelectron spectroscopy (XPS)

was carried out due to obtain an Information about chemical state and electronic state of the elements. SAXS analysis provided information about the depth of cavities which was related to surface area and porosity obtained by BET/BJH methods. Raman scattering was employed to investigate the evolution of the anatase phase in the 2D nanosheets during annealing. The stability of as prepared samples was estimated by Zeta (ζ) potential measurement. UV-Vis analysis and the corresponding photocatalytic performance were evaluated for the degradation of BPA aqueous solutions under UV light irradiation.

2. Materials and methods

2.1 Materials

Titanium (IV) oxysulfate ($TiOSO_4 \cdot xH_2O$, min. 29% Ti as TiO_2, Sigma-Aldrich) served as a titanium precursor. Aqueous solution of ammonia (NH_3, solution purum p.a., 25–29%, Penta) was used for precipitation, and subsequent pH reduction was carried out with the addition of hydrogen peroxide (H_2O_2, solution purum p.a., 30%, Penta). BPA (purity ≥ 99.9%, Sigma-Aldrich) was used as a model compound in photocatalytic experiments. The photocatalytic activity of titanium dioxide Aeroxide® P25 (Evonik) was also tested for the sake of comparison

2.2 Synthesis of aligned 2D TiO_2 Nanosheets

The synthesis of 2D TiO_2 nanosheets was performed by the freeze–drying method and the experimental procedure is shown in Figure 1. The PPTA precursor was synthesized as described in previous publications [29, 36]. Briefly, an aqueous solution of 4.8 g $TiOSO_4$ in 150 mL H_2O was cooled under stirring untill floating ice crystals were formed. Precipitation of the crystals was achieved by dropwise addition of NH_4OH until pH increased above 8. The suspension was kept at 0 °C for 3 h due to aging and the precipitate was then filtered, and washed with distilled water. Following that, the precipitate was treated with 30% H_2O_2 and as a result the color of the suspension changed from white to light yellow and its pH was rapidly decreased to 2. After stirring for 2 h, a transparent yellow precursor solution was obtained. The precursor was then added dropwise into Petri dishes that were filled with liquid nitrogene (LN_2). The frozen droplets were immediatelly transferred into a freeze-dryer and lyophilized at temperature of −64 °C and pressure of 5–10 mTorr until ice was completely removed(~ 48 h). This procedure led to a “popcorn” shaped ultrafine titania composed of thin lamellas of dried gel named Ti_LYO. Precursor Ti_LYO was annealed in air at 500, 650, 800 and 950 °C for 1 h and was easily transformed into vertically aligned arrays of 2D nanosheets composed of platelet – like TiO_2 nanocrystals (NCs). During this step, nanocavities (“nanopockets”) with sharp polyhedral shapes are formed on the surface of TiO_2 NCs and as

a result four new titania materials, namely TiO_LYO_500, TiO_LYO_650, TiO_LYO_800 and TiO_LYO_950, were prepared.

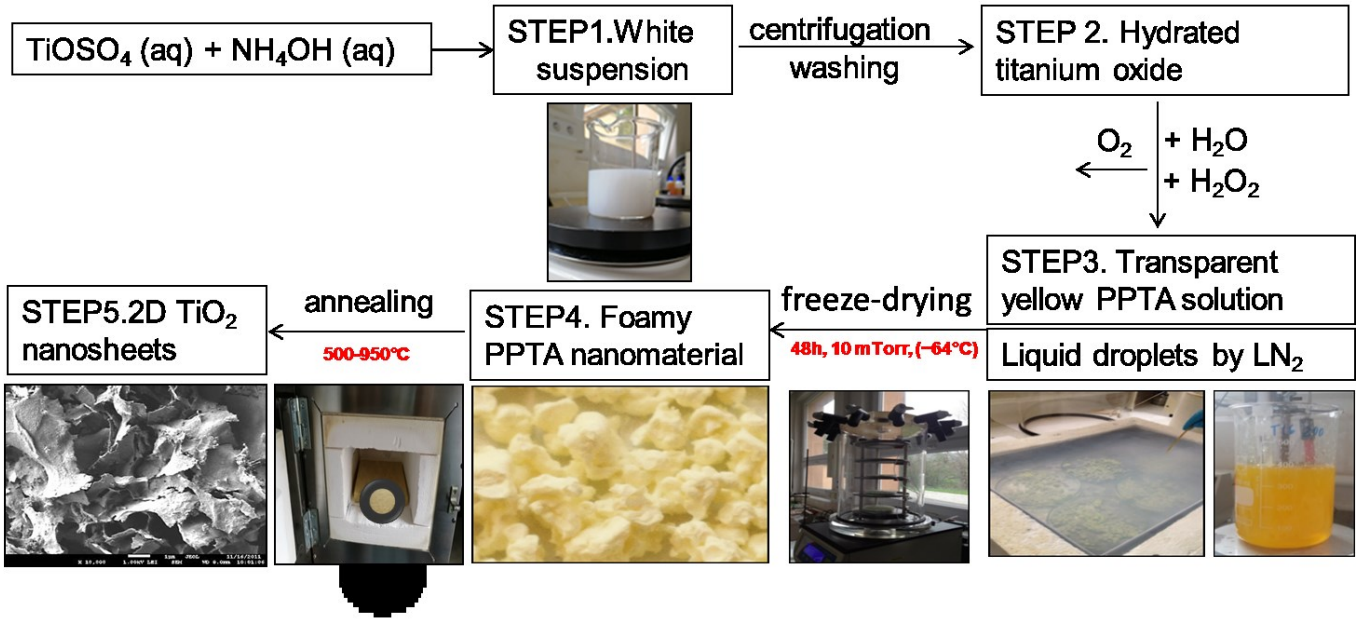

Figure 1. Schematic of the preparation procedure of PPTA precursor and the 2D TiO_2 nanosheets.

2.3 Methods

2.3.1 X-ray powder diffraction (XRD)

Diffraction patterns were collected using a PANalytical XPert PRO diffractometer equipped with a conventional X-ray tube ($Cu_{K\alpha}$ 40 kV, 30 mA, line focus) in transmission mode. An elliptic focusing mirror, a divergence slit 0.5°, an anti-scatter slit 0.5° and a Soller slit of 0.02 rad were used in the primary beam. A fast linear position sensitive detector PIXcel with an anti-scatter shield and a Soller slit of 0.02 rad were used in the diffracted beam. All patterns were collected in 2 theta (2Θ) range of 18–88° with step of 0.013° and 400 s/step dwelling time, producing a scan of about 2.5h. Qualitative analysis was performed with the HighScorePlus software package (PANalytical, The Netherlands, version 3.0e), the DiffracPlus software package (Bruker AXS, Germany, version 8.0) and the JCPDS PDF database [37]. For quantitative phase analysis, DiffracPlus Topas (Bruker AXS, Germany, version 4.2) was used with structural models based on the ICSD database. This program allows the estimation of the weight fractions of crystalline phases by means of the Rietveld refinement procedure. The estimation of the size of crystallites was performed on the basis of the Scherrer formula [38], as implemented within the DiffracPlus Topas software.

2.3.2 Electron microscopy

The morphology of the powdered samples placed on the carbon tape was investigated using a scanning electron microscope (SEM) Philips XL30CP. Measurements were carried out in high vacuum mode (with secondary electrons detector) at accelerating voltage of 25 kV. The samples were observed without coating by the conductive layer to study their original texture. Transmission electron microscopy (TEM) was carried out on a JEOL JEM 3010 microscope operated at 300 kV (LaB_6 cathode, point resolution 1.7 Å) with an Oxford Instruments Energy Dispersive X-ray (EDS) detector attached. Images were recorded on a CCD camera with resolution of 1024 × 1024 pixels using the Digital Micrograph software package. EDS analyses were acquired and treated in the INCA software package. Electron diffraction patterns were evaluated using the Process Diffraction software package [39].

2.3.3 Thermal analysis

Thermogravimetry (TG) and differential thermal analysis (DTA) were performed with the apparatus SetSys Evolution (SETARAM). TA measurements of prepared samples were performed in a crucible made of α-Al_2O_3 in argon flow (60 mL min^{-1}) at atmospheric pressure in temperature range from room temperature (RT) to 1000 °C with heating rate of 5 °C min^{-1}. The dried fine powder (20–25 mg) of TiO_LYO sample was measured.

2.3.4 BET and BJH analysis

Specific surface area was determined by the BET method [40] using a Quantachrome Nova 4200E instrument. Nitrogen adsorption was carried out at −196 °C. The pore size distributions (pore diameter and pore volume) were measured from the nitrogen desorption isotherm using the cylindrical pore model (BJH) [41]. Before measurement, the annealed samples were outgassed for approx. 20 h at 200 °C, lyophilized samples were outgassed for about 35 h at RT.

2.3.5 Small Angle X-ray Scattering (SAXS) experiment

SAXS experiments were performed using a pinhole camera (Older Rigaku SMAX2000 upgraded by SAXSLAB/Xenocs) attached to a microfocused X-ray beam generator (Rigaku MicroMax 003) operating at 50 kV and 0.6 mA (30 W). The camera was equipped with a vacuum version of Pilatus 300K detector. Experimental setup is covering q range of 0.004 – 1.9 $Å^{-1}$. Scattering vector, q, is defined as: $q = (4\pi/\lambda)\sin\theta$, where λ is the wavelength and 2θ is the scattering angle. Calibration of primary beam position and sample-to-detector distances were performed using AgBehenate powder sample. Powder samples were measured in transmission mode between scotch tape. Scotch tape signal was subtracted afterwards. SASView software [42] was used for scattering curves analysis. Most scattering profiles posess similar features, such as small curvature at low-q region, smooth intensity fall

at middle-q region and some background. Intensity in middle-q range is proportional to $q^{-3.9}$, which is close to Porod's law. When no oscillations on scattering curves were observed, a model of polydispersed population of particles comprised of uniform density material and smooth surface was assumed. Usually two populations of particles are observed of which the smaller ones are treated as primary particles and larger ones as aggregates. It is common to describe such particles using mass surface fractal function, where distinct parts of the curve are described using mass fractal or surface fractal functions [43]. In our case, characteristic curvature was observed only for the smaller particles due to SAXS instrument limitations. But describing our system by only mass fractal leads to larger residuals at low-q range.

2.3.6 X-Ray photoelectron spectroscopy

X-Ray photoelectron spectra (XPS) were measured by Kratos ESCA 3400 furnished with a polychromatic Mg X-ray source of Mg Kα radiation (energy: 1253.4 eV). The base pressure was kept at 5.0 10^{-7} Pa. The spectra were fitted using a Gaussian–Lorentzian line shape, Shirley background subtraction and a damped non-linear least square procedure. Survey spectra between 0-1000 eV were collected and more detailed spectra were taken over Ti 2p, O 1s, and C 1s regions. The samples were sputtered with Ar^+ ions at 1 kV with current of 10 μA for 90 sec to remove superficial layers. Spectra were calibrated to C 1s line centered at 284.8 eV.

2.3.7 Raman spectroscopy

Raman spectra were collected by a Nicolet Almega XR dispersive spectrometer equipped with Olympus BX-51 microscope. 128 expositions with resolution 2 cm^{-1} step were taken using excitation wavelength 473 nm.

2.3.8 Zeta potential determinations

TiO_2 samples (0.5 mg) were dispersed in a solvent (10 mL) using ultrasound bath for 10 min. As the solvents distilled water and a 5 mg/L BPA solution in a distilled water were used. The measurements were performed in a BI-SCP cells (10 mm optical path) using a HeNe laser beam 633 nm (NanoBrook Omni, Brookhaven Instruments Corp.). The measurements were repeated five times to check their reproducibility.

2.3.9 UV-Vis diffuse reflectance spectroscopy

The method of UV-Vis diffuse reflectance spectroscopy was employed to estimate band-gap energies of the 2D TiO2 samples. UV-Vis spectroscopy was carried out using a Shimadzu spectrophotometer UV 1800. Reflectance spectra of the solid samples were measured in the range 190 – 550 nm using a PTFE as a standard. Kubelka-Munk transformation was then

applied and Tauc plots were used to calculate band gaps of the material [34/47]. The band-gap energy Ebg was calculated by the extrapolation of the linear part of equation λbg = 1240/Ebg (eV) [49, 50].

2.3.10 Photocatalytic activity test

Photocatalytic experiments were carried out using BPA as the model compound to evaluate the photocatalytic activity of the newly synthesized materials. The experiments were conducted in a batch-operated slurry photoreactor, applying a working volume of 150 mL. Irradiation was provided by a UVA light-emitting diode (LED) (λ_{max}=365 nm; LZ4-00U600, LED Engin) driven by electrical power of 11 W. The emitter was mounted onto a heat sink to prevent radiant flux decrease due to temperature rise. The LED assembly was placed directly above the reactor and a quartz protective plate was placed between them to protect the lamp from water spills. The photocatalytic set-up was covered with an aluminium shield to prevent light diffusion out of the reactor and to minimise penetration of ambient light. In a typical run, BPA solution was loaded in the photoreactor and the appropriate amount of catalyst was added. The obtained slurry solution was continuously stirred magnetically at 500 rpm to promote uniform suspension of catalyst powder and dissolved oxygen. At the beginning of each experiment, the solution was stirred in the dark for 30 min considering that a well-adsorbed substrate is more likely to be oxidised by the short-life photogenerated holes on catalyst surface [44]. The UV source was then switched on and at regular time intervals samples were withdrawn and filtered through 0.45 μm polyvinylidene fluoride syringe filters (CM Scientific Ltd) to remove catalyst and further analysed in terms of BPA concentration. The incident photon flux received by the reactant solution was determined by potassium ferrioxalate actinometry, as described by Murov [45] and was estimated at $3.32 \cdot 10^{-6}$ Einstein/s. During treatment, the temperature of the reactant solution was left uncontrolled, presenting a variation between 24 – 26 ^{o}C. All experiments were conducted at the inherent pH of BPA solution (~ 6.9), which remained constant during photocatalytic treatment.

BPA concentration in filtrate samples was measured by a high performance liquid chromatography (HPLC) system (S200 Pump, S225 Autosampler, Perkin Elmer) coupled with a diode array detector (S200 EP, Perkin Elmer). Samples were separated by reverse phase (RP) chromatography using a C18 Luna (Phenomenex) column (5u, 250 x 4.6 mm). The mobile phase was a mixture of 35:65 UPW:acetonitrile fed at a flow rate of 1 mL/min [46]. The solvents were eluted isocratically and the injection volume was 40 μL. The detection wavelength was at 225 nm. BPA degradation was fitted to the pseudo-first-order kinetic model:

$$\ln\left(\frac{C}{C0}\right) = -kt \quad (1)$$

where C and C_0 are BPA concentrations at time t and t = 0, respectively, and *k* is the pseudo-first-order kinetic rate constant [47,48].

3. Results and discussion

3.1. Characterization of 2D-TiO_2 nanosheets

3.1.1. Microstructure and morphology

Fugure 2 shows powder X-ray diffraction patterns of as-prepared solid samples TiO_LYO_500, TiO_LYO_650, TiO_LYO_800, TiO_LYO_950 and lyophilized precursor TiO_LYO. The observation of 2θ value at 18.5° and 42.64° can be attributed to the Mylar foil, which was used as the sample holder.

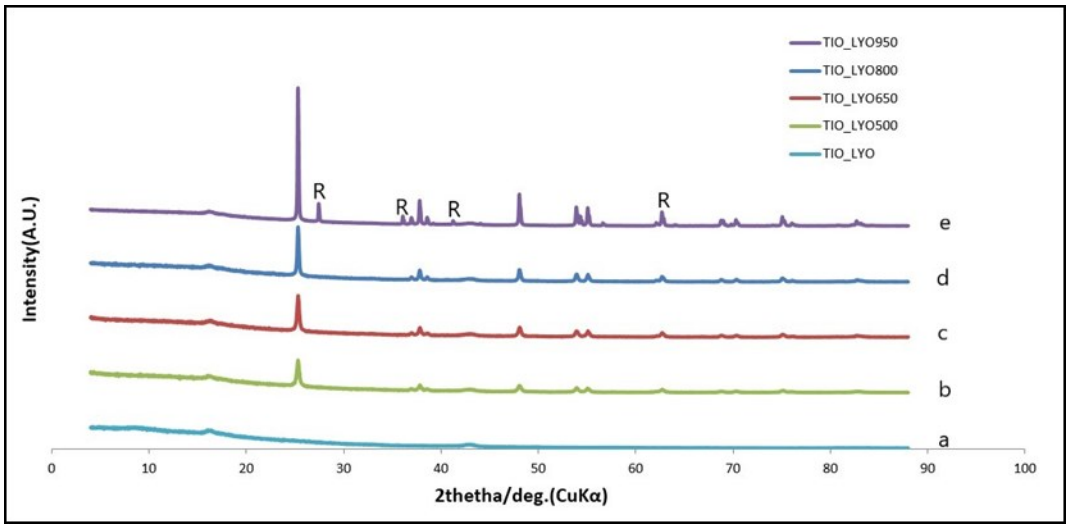

Figure 2. X-ray diffraction patterns of (a) the precursor TiO_LYO and its post-synthesis heat treatment (b) the sample TiO_LYO_500, (c) the sample TiO_LYO_650, (d) the sample TiO_LYO_800 and (e) the sample TiO_LYO_950.

The raw freeze-dried precursor TiO_LYO was identified as strictly amorphous material (curve a). The XRD pattern of sample TiO_LYO_500 annealed at 500 °C (curve b) corresponds to tetragonal anatase phase (ICDD PDF 21-1272) [37]. We can follow the increase of the intensity of anatase peaks (curve c) up to annealing temperature 800 °C (curve d). The thermal treatment of the amorphous freeze-dried PPTA precursor led to spontaneous crystallization and controlled anatase-rutile transformation. Sample TiO_LYO_950 (curve e) contains 14.46 % rutile phase (ICDD PDF 21-1276). It should be noted that our results are in agreement with previously reported observations [51]. The average size of anatase and rutile crystallites was calculated using Scherrer equation. The continuous growth of crystallite size was determined for all heat treated samples. Calculated lattice parameters are also

presented in Table 1. It is observed that lattice parameter *a* decreases since lattice parameter *c* increases due to possible distortion and strain induced in TiO_2 lattice during annealing. It can be suggested that both apical (Ti-O-Ti) and equatorial (O-Ti-O) bonds in the TiO_6 octahedron primitive cell are changed and disballance in the electric charge in Ti-O bonds could be formed by introducing oxygen vacancies into their vicinity.

Table 1. Microstructural parameters of samples TiO_LYO_500, TiO_LYO_650, TiO_LYO_800, TiO_LYO_950 obtained by XRD analysis.

Sample	Phase composition	Anatase form XRD	Rutile form XRD	Anatase crystallite size	Rutile crystallite size	Anatase lattice parameters [Å]		Rutile lattice parameters [Å]	
		[%]	[%]	[nm]	[nm]	*a, b*	*c*	*a, b*	*c*
TiO_LYO	-	0	0	-	-	-	-	-	-
TiO_LYO_500	A*	100	0	9.2	-	3.7857	9.5104	-	-
TiO_LYO_650	A	100	0	11.7	-	3.7847	9.5111	-	-
TiO_LYO_800	A	100	0	18.4	-	3.7846	9.5123	-	-
TiO_LYO_950	R**	84.54	14.46	111	149.1	3.7844	9.5120	4.5934	2.9585
Degussa_P25	A + R	83	17	20.8	30.5	-	-	-	-

*A=anatase, **R=rutile

According to previous studies [29,36] freeze-drying procedure leads to the formation of TiO_2 nanomaterial with lamellar structure. The morphology of sample TiO_LYO is presented in Figures 3a (low magnification) and 3b (high magnification). An individual lamella has thickness below 50 nm, with a large lateral size in the order of tens of microns. The layers are folded into dense multilayered spherulites with common spheroidal core (see inset in Figures 3a-b), which is formed when the reaction solution is dripped in small droplets into liquid nitrogen before the freeze-drying process (Figure 1/step 3). One possibility is that phase separation of highly supersaturated liquid droplets that subsequently undergo PPTA mediated crystallization can produce the concentrically layered spheroids. As the process occurs within droplets of confined volume, 3D radial-structured porous shells were formed. It was determined that as-obtained spheroidal agglomerates consist of thin leaves when sample TiO_LYO was annealed at 500 °C (Figure 3c). Figures 3d and 3e show the SEM images of sample TiO_LYO grown for 1 h at 650 and 800 °C, respectively. The joined crystalline lamellas can be observed at temperatures up to 800 °C (Figure 1e). Such lamellar morphology is a result of the controlled nucleation in freeze-drying procedure, which affects the phase morphology and stablity of samples [51]. The TiO_2 sheets are well separated without a bending and crumpling and tend to be vertically aligned. The crystallization takes place only in 2D direction while the lamellar structure with different degrees of crystallinity is preserved. Such morphology has the advantage of preventing agglomeration and thus

enables the formation and preservation of a high surface area [29, 36]. The branching phenomenon of TiO_2 nanosheets is registered at the temperature of 950 °C (Figure 3f); the lamellar morphology partly collapsed since anatase-rutile transformation took place (see XRD part and Table 1). The samples TiO_LYO_500, TiO_LYO_650, TiO_LYO_800, TiO_LYO_950 are very pure and contain only Ti and O (Figure S1). The EDS analysis shows no traces of contaminations; the samples were completely free from SO_4^{2-} and N_2-residuals which could come from the initial reactants ($TiOSO_4$ or NH_4OH, respectively). A really small Si peak (i.e. below quantification limit) was also detected probably due to tiny contamination.

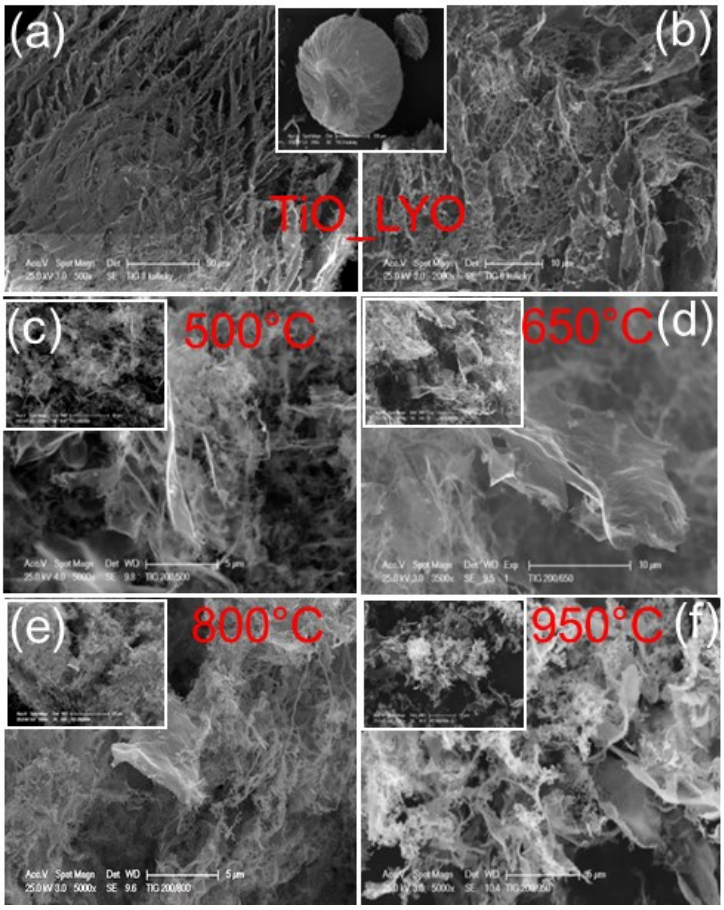

Figure 3. SEM graphs of (a) lyophilized precursor TiO_LYO at Low and (b) High Mag showing nanosheet morphology; (c) Low Mag of sample TiO_LYO obtained at 500 °C and High Mag in the inset; (d) Low Mag of sample TiO_LYO obtained at 650 °C and High Mag in the inset; (e) Low Mag of sample TiO_LYO obtained at 800 °C and High Mag in the inset; (f) Low Mag of sample TiO_LYO obtained at 950 °C and High Mag in the inset.

High resolution transmission electron microscopy (HRTEM) was used to study the detailed morphology of individual 2D TiO_2 nanosheets as well as their structure using selected-area electron diffraction (SAED). TEM image of sample TiO_LYO presented in Figure 4a confirms

that individual layers are formed during freeze-drying process. Such obtained pristine sample does not show cavities or irregular features on its surfaces.

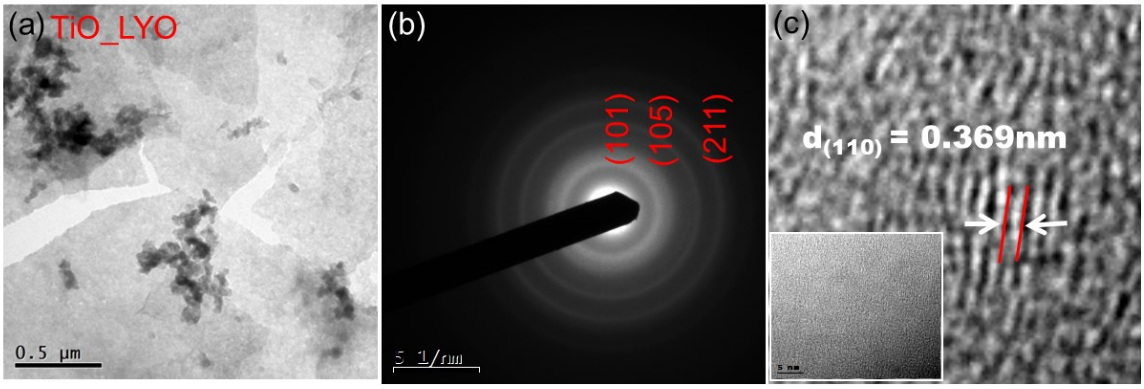

Figure 4. (a) TEM image of pristine sample TiO_LYO (b) SAED pattern of TiO_LYO indexed to the orthorhombic hydrogen titanium oxide hydride $H_4Ti_2O_6.H_2O$ (c) HRTEM image of TiO_LYO with interlayer distance *d* confirms $H_4Ti_2O_6.H_2O$ structure.

The layers have size of several tens of micrometers and thickness judged from the TEM image only about 10 nm. The SAED patterns (Figure 4b) yields three rings indexed to the (101), (105) and (211) diffraction lines, respectively, of the orthorhombic hydrogen titanium oxide hydride (PDF ICDD 47-0124). The HRTEM image (Figure 4c) indicates ~ 5 nm highly crystallized $H_2Ti_nO_{2x+1-x}H_2O$ nano-islands that we indexed as 0.369 nm distance to $d_{(110)}$ of an $H_4Ti_2O_6$ hydrogen titanate [51]. Further, we investigated the temperature dependence of morphological evolution and the corresponding properties variation of the TiO_LYO 2D sheets upon thermal annealing for 1 h at different temperatures ranging from 500 to 950 °C (Figure 5). A remarkable property of these heat-treated 2D materials is related to the crystal surface of samples TiO_LYO_500, TiO_LYO_650, TiO_LYO_800 and TiO_LYO_950. It can be seen that 2D TiO_2 nanosheets are mainly composed of closely packed planar nanocrystals with regular size that ranges from 40 to 77 nm in both length and width (Figures 5a-5d). Overall, TEM observations show that the nanocrystals are single crystals with similar shape and size distributions. Unlike the pristine precursor TiO_LYO (Figure 4a), we observe numerous polyhedral nanocavities inside the TiO_2 planar crystals, as shown in both low (Figures 4a-4d) and high (Figures 4a1-4d1) magnification TEM images. The SAED patterns corresponding to the samples heat-treated at 500 °C (Fig. 5a/inset), 650 °C (Figure 5b/inset) and 800 °C (Figure 5c/inset) are indexed on the basis of the tetragonal anatase TiO_2 with space group $I4_1/amd$ and lattice parameters a = b = 0.378 nm and c = 0.951 nm (ICDD PDF 21-1272). These results are in agreement with previously reported observations [29,36,51] and are complemented by XRD measurements. The measured interlayer spacing was found

to be $d_{(101)}$ = 0.352 nm for samples TiO_LYO_500 and TiO_LYO_650 (see HRTEM micrographs presented in Figures 4a2 and 4b2). The dehydration process during heating in air leads to a slight decrease of the interplane spacing of the sheets to 0.349 and 0.345 when the temperature reaches 800 and 950 °C, respectively (see HRTEM micrographs in Figures 5c2 and 5d2). The results indicate that most of the water confined in 2D TiO_2 nanosheets is removed by heating them to 950 °C. The SAED pattern of sample annealed at 950 °C (Figure 5d1/inset) presents extra diffraction spots, which belong to the rutile TiO_2 phase (ICDD PDF 21-1276). The transformation of anatase to the stable rutile polymorph reportedly occurs at temperatures slightly above 600 °C [52]. In this work, the transition begins at about 900 °C. The electron diffraction study demonstrates high temperature structural stability of as-obtained 2D TiO_2 nanostructures. Since in many practical applications the reaction temperatures are higher than the ambient, the thermal stability of catalysts has to be taken into account. The bright-field HRTEM images taken at low magnification (Fig.S2) showed fine intergrowth TiO_2 nanocrystals of various sizes and shapes, closed-packed into a single 2D nanosheet [29]. These results had corroborated the XRD outcomes (Table 1). The HRTEM/SAED study demonstrates the high temperature structural stability of as synthesized samples and their potential application in catalytic reactions requiring high operating temperatures.

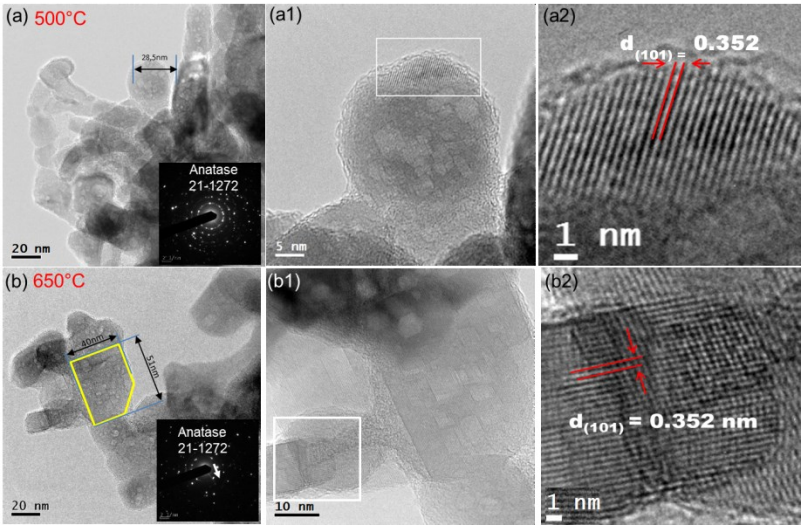

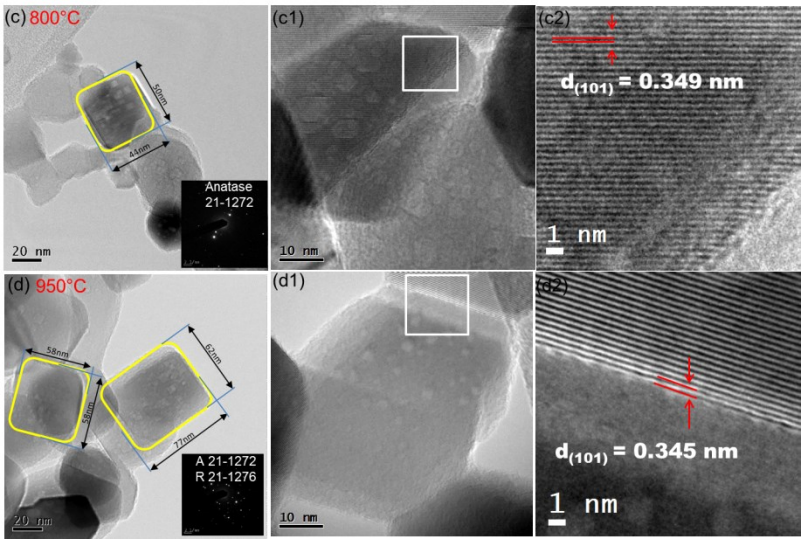

Figure 5. TEM observations of (a) TiO_LYO_500 at Low Mag, the inset shows the diffraction pattern obtained from the FFT study of the tetragonal anatase (a1) High Mag showing single anatase crystal containing arrayed nanocavities; (a2) HRTEM image from white boxed area with interlayer distance of anatase image (b) Low Mag ofTiO_LYO_650, the inset shows the diffraction pattern obtained from the FFT of the tetragonal anatase (b1) High Mag showing single anatase crystals containing arrayed nanocavities (b2) HRTEM image from white boxed area with interlayer distance of anatase image (c) Low Mag of TiO_LYO_800, the inset shows the diffraction pattern obtained from the FFT of the tetragonal anatase (c1) High Mag showing single anatase crystals containing arrayed nanocavities (c2) HRTEM image from white boxed area with decreased interlayer spacing of anatase image (d) Low Mag of TiO_LYO_950, the inset shows the diffraction pattern obtained from the FFT of the tetragonal anatas and tetragonal rutile (d1) High Mag showing intergrown crystal grains (d2) HRTEM image from white boxed area with decreased interlayer spacing of anatase image.

As can be seen in the high-magnification image with incident beam along the [100] direction (Figure 6a), when sample TiO_LYO_500 comprising only anatase TiO_2 nanocrystals is viewed along the principle [100] direction, many nanocavities with a sharp polyhedral shape are observed, The contrasts in the HRTEM image of sample TiO_LYO_650 (Figure 6b) can be easily identified corresponding to the main directions of the anatase type unit cell. When the image contrast is carefully observed in Figure 6c , the presence of the polyhedral cavities in sample TiO_LYO_800 can be deduced. However, they are better observed in a slightly tilted orientation and under out-of-focus conditions. These appear as merged hollow cages “nanopockets” (their nature will be further explained) and are well oriented polyhedra with faces parallel to [010] and [001] in the [100] projection. The electron diffraction pattern taken from the whole nanocrytsal (inset of Figure 6c) was indexed as the (100) pattern of anatase, indicating that the planar nanocrystal is still a single crystal anatase phase. The typical size of the nanocavities ranges from 5 to 10 nm in both length and width (Figures 6a – 6c). HRTEM image of sample TiO_LYO_950 (Figure 6d) shows (101) faces of tetragonal rutile structure with a space group $P4_2/mnm$ (ICDD PDF 21-1276) (inset graph of Figure 6d). As

reaction temperature increases, rutile nanocrystals start to nucleate and grow along the grain boundaries of anatase. Sharp polyhedral nanocavities occur towards [001] direction as can be observed in Figure 6d.

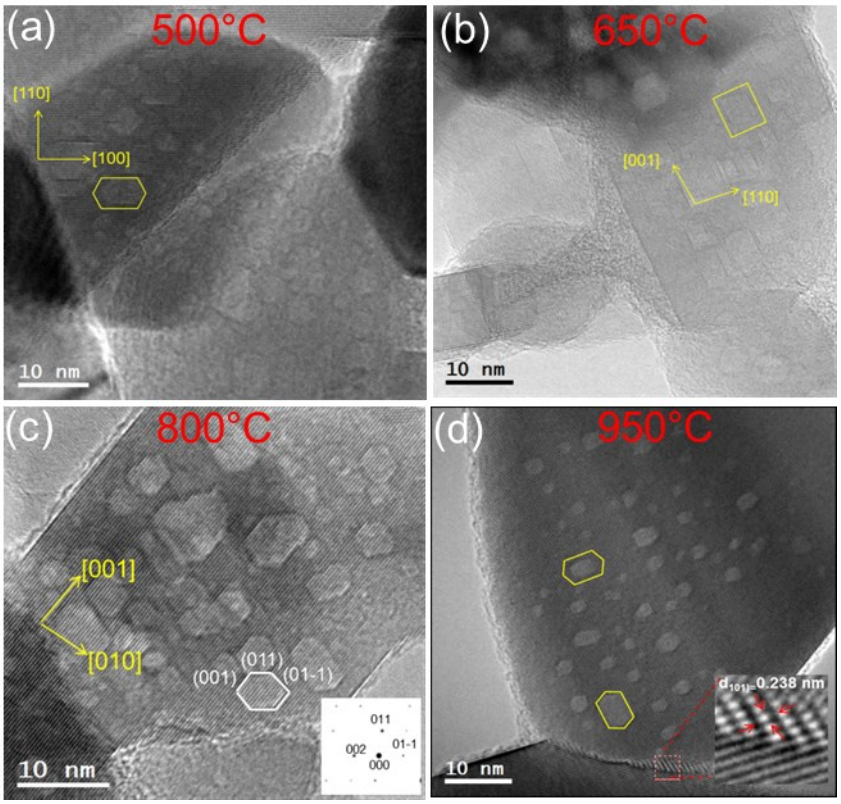

Figure 6. HRTEM observation of nanocavities (a) TiO_LYO_500 anatase crystals along the [100] direction (b) TiO_LYO_650 anatase crystals along [010] projection (c) TiO_LYO_800 anatase crystals along [001] projection (d) TiO_LYO_950 rutile crystals with (101) plane.

3.1.2 Thermal analysis

The as-synthesized materials were further investigated by thermal analysis. Sample TiO_LYO passes through different thermal transformations in the temperature range of RT-1000 °C, as shown by the corresponding thermal analysis (Figure 7). It is known that in the titania precursor prepared by using H_2O_2, the decrease of the emanation rate ranging from 650 to 750 °C [53] is a main characteristic of the microstructure of the material after PPTA precursor degradation. It is suggested that tetrahedral ammonium departs from the structure in three overlapping steps between 250 and 500 °C. The first step might be weakly bonded ammonium closer to the surface, which evolves together with water up to 200–250 °C. The next step occurrs at temperatures up to 500 °C, evidencing that ammonium located in the nanopores (nanotunnels) of TiO_2 structure is fully eliminated [54]. In addition to the

endothermic peak at 80–90 °C, assigned to the first evolution of water, two other broad peaks are observed between 200 and 500 °C in agreement with previous report [55]. Therefore, we can accept that the first step in the weight loss occurs at a temperature about 200 °C, and around this temperature the tunnels start to empty and previous structures begin to transform into the final tetragonal anatase. According to HRTEM studies, it is exactly above this temperature when nanocavities appear on the surface of the TiO_2 crystals. This is consistent also with the fact that pristine sample TiO_LYO does not show cavities or irregular features on its surface.

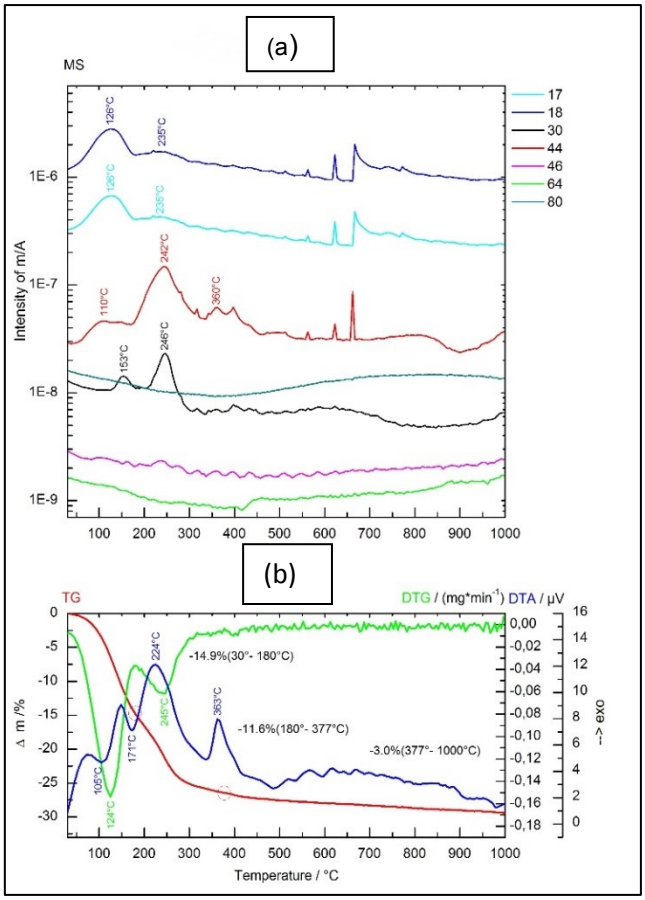

Figure 7. MS and DTA/TG curves of the pristine sample TiO_LYO.

3.1.3 Surface properties of 2D TiO_2 nanosheets – BET and BJH measurement

Detailed BET/BJH hysteresis graphs for cryo-lyophilised samples can be found in our recent publication [56]. Samples heated at 500, 650, 800 and 950 °C exhibit obvious hysteresis behavior, indicating that the products are mainly mesoporous according to IUPAC classification [57]. Table 2 shows pore structures calculated according to the adsorption BET/BJH data.

Table 2. Surface area, porosity, band-gap energy E_{bg}, rate constants k and zeta potential of samples TiO_LYO, TiO_LYO_500, TiO_LYO_650, TiO_LYO_800, TiO_LYO_950.

Sample	BET [m^2g^{-1}]	BJH [$cm^3\ g^{-1}$]	Average pore size [nm]	Rate constant k [min^{-1}]	Band gap eV	Zeta potential [mV] H_2O	Zeta potential [mV] BPA/ H_2O
TiO_LYO	126	0.301	10.1	-	3.19	-17.4	- 23.3
TiO_LYO_500	64.0	0.130	4.89	0.0279	3.24	-18.4	- 22.5
TiO_LYO_650	50.5	0.049	4.10	0.0381	3.24	-14.5	- 21.6
TiO_LYO_800	25.5	0.028	5.5	0.2539	3.24	-18.9	- 23.2
TiO_LYO_950	11.6	0.018	2.40	0.1796	3.23	-24.8	- 25.1
Degussa_P25	50.0	-	-	0.1106	3.19	+15.6	-5.6

The specific surface areas of the pristine sample TiO_LYO and samples annealed at 500 and 650 °C are high in comparison to the standard material Degussa P25 [58], which has a surface area of ca. 50 m^2/g. The surface area decreases with the synthesis temperature and reach a maximum of 64 m^2/g at 500 °C. Sample TiO_LYO_650 has surface area similar to those reported for P25 and after this temperature (i.e. 650 ^oC), the surface area is decreased with temperature increasing up to 950 °C. Pore volume becomes maximum at 500 °C. The BJH method was also employed to analyze the pore size distributions and the results are shown in Table 2. It can be observed that the distributions are very narrow, ranging between 2.4 and 10 nm. The decrease in surface area or pore volume with the treatment temperature in the regime (<800 °C) can be attributed to the enhanced rupture of Ti-O-Ti bonds in the TiO_2 nanoparticles to form Ti-OH bonds [59]. The rupture leads to the formation of lamellar TiO_2 sheets because of the electrostatic repulsion of the charge on Ti-O-NH_4. These results are coherent with our SEM observations where 2D titania nanosheets without scrolling can be seen (Fig. 3). In the case of heat treatment from 500 to 950 °C, the N_2 adsorption-desorption isotherm was found to be typical of the H3-type hysteresis [60] loops in IUPAC classification [61] indicating that the TiO_LYO_500, TiO_LYO_650, TiO_LYO_800 and TiO_LYO_950 materials consist of platelike particles [51]. No heat treatment may result in a negligible extent of bond rupture, forming lamellar sheets thicker than the platelike crystals obtained at higher treatment temperatures. The sheets (and plates) cannot scroll to become nanotubes after NH_4OH and H_2O_2 treatment since there is no rapid removal of electrostatic charges. The peak pore size of ca. 4 nm in the BJH analysis may represent the average interval between the platelike particles.

3.1.4 Small-angle scattering studies (SAXS)

SAXS have been applied to investigate the nanotexture of 2D TiO_2 nanosheets. Unannealed samples TiO_LYO and TiO_LYO_500 exhibit similar R_g values of smaller particles, about 81 Å. This value is higher for the samples annealed at higher temperatures. R_g values were 151 Å and 202 Å for the samples TiO_LYO-650 and TiO_LYO 800, respectively, while R_g > 1000 Å was obtained for the sample TiO_LYO_950. Results from SAXS expriment are in line with XRD calculations for TiO_2 crystallite size shown in Table 1 and confirm the complementarity of the two methods.

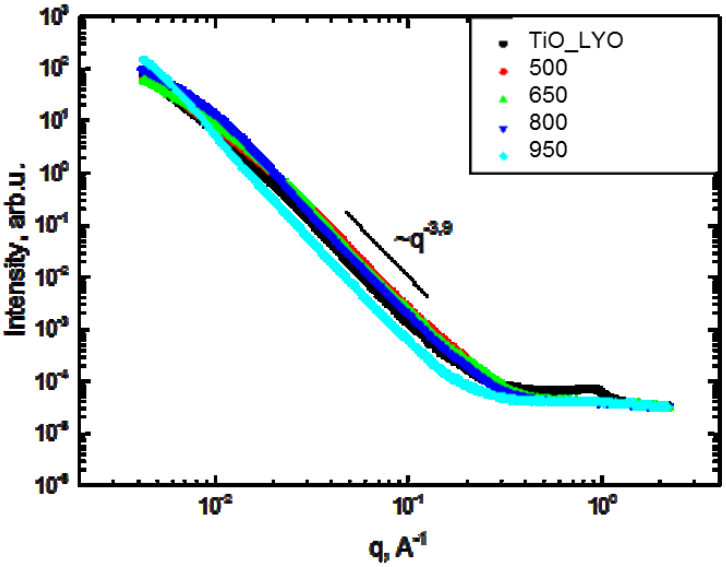

Figure 8. Small-angle X-ray scattering profiles for samples TiO_LYO, TiO_LYO_500, TiO_LYO_650, TiO_LYO_800 and TiO_LYO_950.

On the other hand, the behaviour of the as-synthesized samples is different from that observed by Notestein's group [62] for metal nanoparticles with nanocavities. In this work data are fitted using the fractal model, which does not represent any particular shape but allow for the estimation of porosity and the sizes of pores. The best scattering curve that exhibits significant feature is that measured for sample TiO_LYO_800 in lower angles. Interestingly, the lowest value of mass fractal dimension was found for sample TiO_LYO_650, indicating more porous structure at 650 °C. This behaviour can be explained by the well-known fact that bringing a nanotextured surface into contact with water, results in a sensible reduction of electron density contrast (and therefore of the scattered X-ray

intensity) if the liquid penetrates significantly into the cavities. Therefore it can be suggested that hydrophobic surface of samples TiO_LYO_650 leading to decrease of the integrated scattered X-ray intensity after the surface were put in contact with water. HRTEM micrographs in Figures 5b1 and 6a show surface patterned with nanocavities whose depth could be estimated by penetration of water into the cavities. Therefore, empty nanotunnels will be formed after releasing of the confined water [63]. Fitting of the results was made by SASFit software [64] and is presented in Figure 8. The parameters obtained are R_g = 270 Å and D = 3.59; the latter related to the smoothness of the surface with its calculated value (~3) represents 3D structures. Since the maximum dimension for D is about 4, it can be assumed that the surface of 2D TiO_2 nanosheets heated from 650 to 950 °C is not perfectly smooth due to self-assembled densely packed hydrophobic nanocavities on their surface.

3.1.5 X-ray Photoelectron Spectroscopy (XPS)

XPS was used to analyze surface stoichiometry and valence state of the prepared materials. The surface spectrum revealed only titanium, oxygen and carbon in the superficial layers. No other elements were detected by analyzing surface spectra in a range 0-1000 eV. Ti 2p, O 1s and C 1s regions were then collected with higher resolution and analyzed. The new materials were found to contain only $Ti^{(4+)}$ at surface (458.9 and 464.8 eV). After sputtering, the Ti 2p lines broadened due to removing the surface TiO_2 and new bands proving lower oxidation states were observed. After Shirley background subtraction and deconvolution, the spectra give rise to five components as shown in Figure 9a.

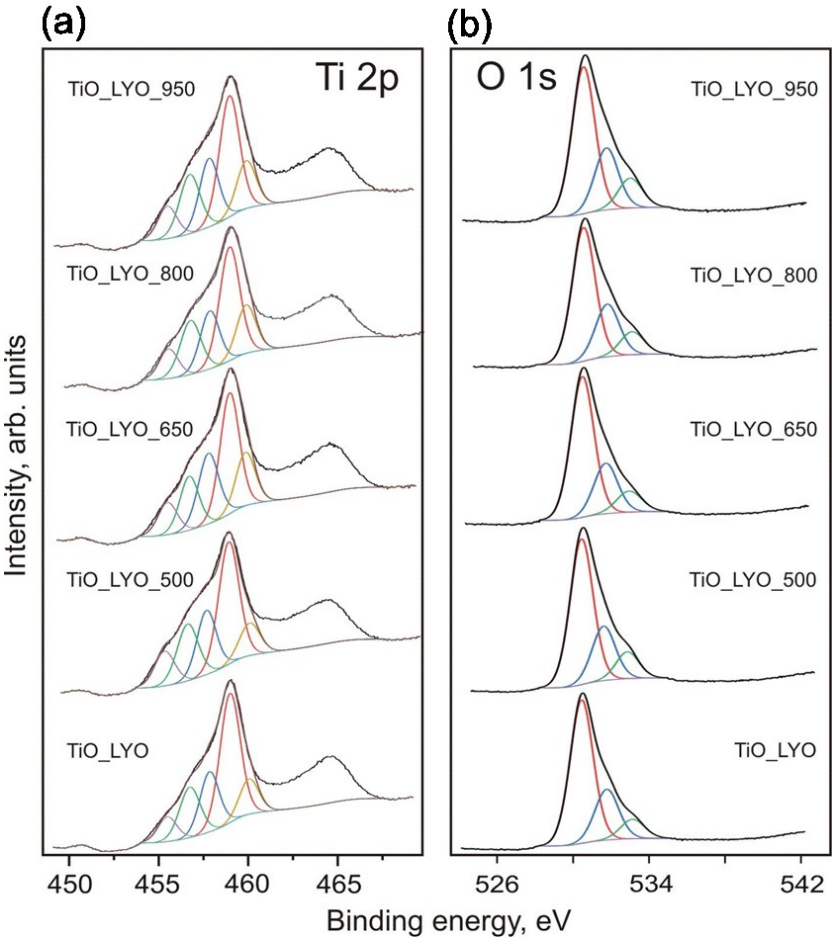

Figure 9. (a) Ti 2p and (b) O 1s XPS spectra of samples TiO_LYO, TiO_LYO_500, TiO_LYO_650, TiO_LYO_800 and TiO_LYO_950.

The most intense Ti $2p_{3/2}$ band is ascribed to $Ti^{(4+)}$, but lower binding energy ones are $Ti^{(3+)}$ contributions in nonstoichiometric oxides (457.7 and 456.7 eV), while the lowest binding energy 455.4 eV is typical for $Ti^{(2+)}$. On the other hand, the band above 460 eV should be ascribed to titanium atoms bonding to hydroxyl groups.

O 1s region (Figure 9 b) contains bands from titanium oxides and this contribution is fitted by a broader band centered at about 530.4 eV. Higher binding energy bands are attributed to hydroxyl groups bonding to titanium atoms (531.6 eV) and from carbon moieities (carbonyl and carboxyl groups) and adsorbed water.

Detailed examination of N 1s region revealed no presence of nitrogen in the sample. NH_4OH used for hydrolysis of titanyl sulfate was completely washed off and this means that no nitrogen residuals were observed in the final materials. This is also confirmed by the EDS analysis, which shows only Ti and O_2 in all samples (Figure S1). Only lyophilized precursor TiO_LYO exhibits yellowish colour (see a flow diagram in Figure 1), whereas annealed samples TiO_LYO, TiO_LYO_500, TiO_LYO_650, TiO_LYO_800 and TiO_LYO_950 are typical white TiO_2. (Figure S3).

3.1.7 Raman spectroscopy

The Raman spectra, collected by a micro Raman technique, show presence of the anatase TiO_2 form (Figure 10) evidence by typical bands centered between 142 and 639 cm^{-1}. Even at the highest temperature (950 ^oC) the spectrum did not prove presence of rutile as revealed by XRD analysis due to much weaker cross-section of the rutile form in comparison with anatase due to excitation by visible laser beam. For comparison, Raman spectrum of the Degussa P25 was collected, in which anatase bands and weak contributions of the rutile form present at 442 cm^{-1} (broad band) and 611 cm^{-1} (shoulder) can be identified. This can be attributed to the higher content of rutile form in the sample.

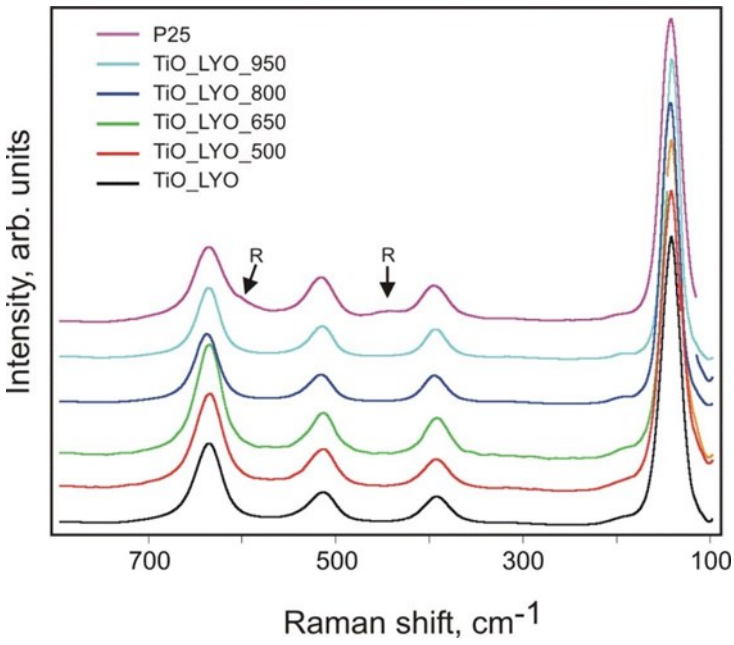

Figure 10. Raman spectra of the samples TiO_LYO, TiO_LYO_500, TiO_LYO_650, TiO_LYO_800 and TiO_LYO_950 and P25.

3.1.6 Optical properties and energy band composition

Spectra in the UV-Vis region were measured by a reflection technique and reveal high difference in reflectivity in visible and UV regions (Figure 11). The spectra of the precursor Ti_LYO and annealed samples (500 – 800 °C) show similar reflectivity with the same slope. Presence of the rutile form in the Ti_LYO_950 and P25 leads to a shift of the spectra to higher wavelengths. The reflection spectra were transformed by a Kubelka – Munch

procedure to calculate band gaps of the as-prepared material. The results are presented in Table 2.

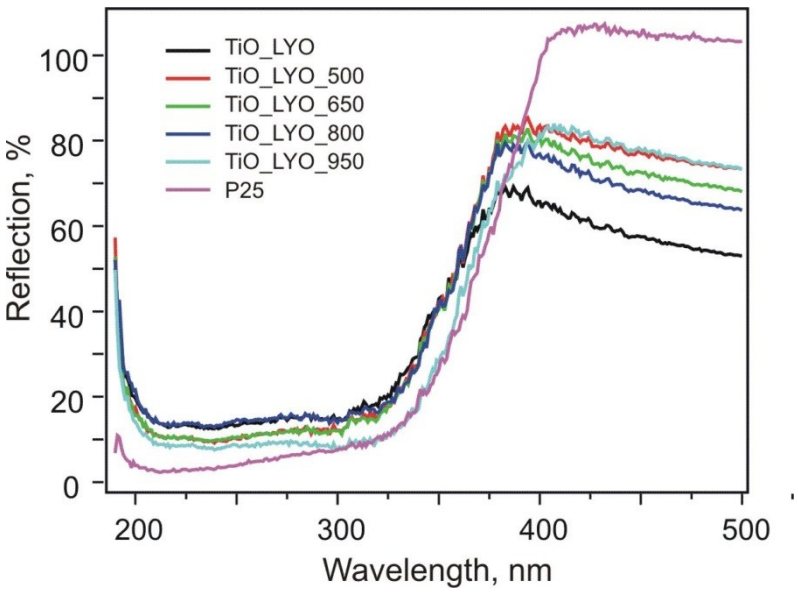

Figure 11. UV-Vis reflection spectra of the samples TiO_LYO, TiO_LYO_500, TiO_LYO_650, TiO_LYO_800 and TiO_LYO_950 and P25

3.2 Photocatalytic activity

3.2.1 Zeta potential (ZP) determinations

The as-prepared materials TiO_LYO, TiO_LYO_500, TiO_LYO_650, TiO_LYO_800 and TiO_LYO_950) were dispersed in a BPA solution and the suspensions were intensely stirred. To evaluate the stability of the suspensions their ZP was measured. Blank measurements in distilled water were carried out. It was found that ZPs are in the range of -14.5 to -24.8 mV (see Table 2), which shows that suspensions are not completely stable. The ZP of the as-prepared samples are shifted several mV to lower potentials and these results prove the positive role of BPA molecules in the stabilization of the suspensions. On the other hand, the same measurement with P25 resulted in +15.6 mV ZP suspensionin the blank suspension and a much more pronounced shift (to -5.6 mV) in the BPA suspension. These suspensions were more unstable and faster separation of solid particles from the liquid BPA solution occured. ZPs of the BPA suspensions correlate to higher affinity of samples annealed at 800 and 950 ^{o}C to BPA (Figure 12) as shown by lower BPA/BPA$_0$ values. Similar ZP of the as

prepared sample, but its lower affinity towards BPA can be explained by higher carbon content in the sample, which is known to stabilize suspensions.

3.2.2 Photocatalytic decomposition of BPA

To evaluate the relative activity of the as-prepared 2D TiO_2 catalysts with cavitated nanosheet morphology, experiments were carried out at 5 mg/L BPA initial concentration and 200 mg/L catalyst loading. The results are shown in Figure 12, where it can be observed that the highest BPA removal is obtained in the presence of TiO_LYO_800 followed by TiO_LYO_950, TiO_LYO_650 and TiO_LYO_500 catalysts. In addition, an experiment was performed in the presence of TiO_2-P25 photocatalyst, at the same operating conditions, to establish a comparison against commercially available catalysts. It was observed that TiO_LYO_800 and TiO_LYO_950 catalysts yielded higher efficiency in terms of BPA degradation than TiO_2-P25 standard. Rate degradation constants are presented in Table 2.

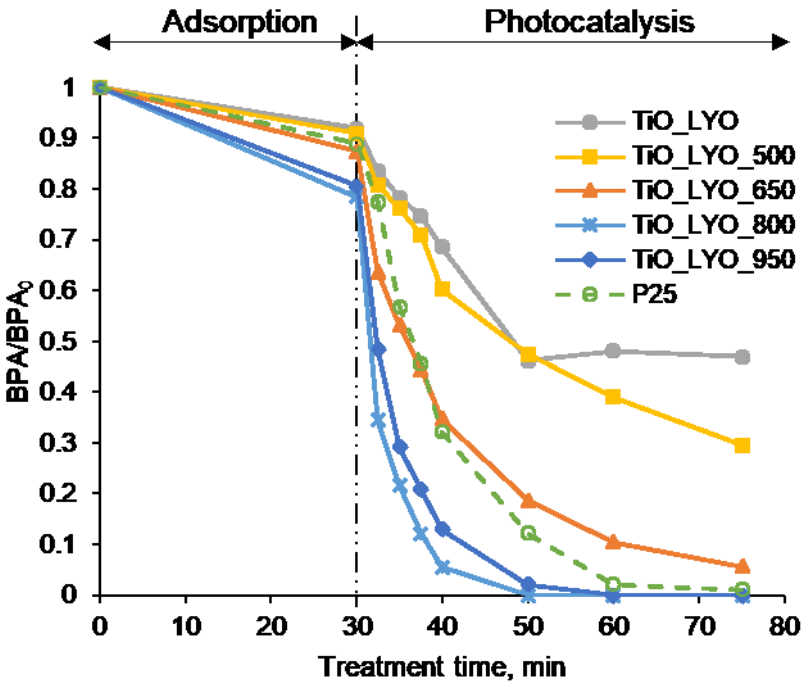

Figure 12. Photocatalytic degradation of BPA in the presence of TiO_LYO, TiO_LYO_500, TiO_LYO_650, TiO_LYO_800, TiO_LYO_950 and Degussa P25 catalysts.

The values of band gaps are also listed in Table 2. The blue shift of the absorption edge of samples TiO_LYO_650, TiO_LYO_800 and TiO_LYO_950 towards higher energies and leads to widening of the band gap of up to 0.05 eV (or 0.04 eV in case of sample TiO_LYO_950) compared to the P25 reference catalyst. This blue shift cannot be rationalized based on previous reports that observed that with decreasing crystallite size the

optical edge tended to shift to higher energy [65,66], , since in this work increasing of the temperature leads to a linear increase of the particle size (see Table 1). The results of X-ray powder patterns reveal that the crystal lattice of samples TiO_LYO_500, TiO_LYO_650, TiO_LYO_800, TiO_LYO_950 slightly expanded with an increase in growth temperature. The disballance in the electric charge in Ti-O bands could be introducing intrinsic local atomic defects such as oxygen vacancies [67].

The blue shift in the absorption edge and widening of the band gap can be explained on the basis of lattice expansion and this may hint to the contribution of intrinsic defects in TiO_LYO_500, TiO_LYO_650, TiO_LYO_800, TiO_LYO_950 catalysts. Therefore, this indicates that increasing of the band gap could be connected with lattice expansion in annealed materials [68-70]. On the other hand, thermal annealing does not eliminate the native defects (nanocavities) on the surface of the material even at high annealing temperatures (i.e. 950 °C). Self-assembled densely packet nanocavities with size range from 5 to 10 nm in both length and width, and depth of about 3.6 nm (material TiO_LYO_800) are responsible for the enhacenemet of the optical absorption, and therefore the photocatalytic activity (Figure 12). In addition, the nanocrystallinity has improved since annealing above 500 °C is a fundamental requirement for the complete decomposition of the TiO_LYO precursor as well as for optimizing the high crystallinity, preventing the formation of clusters and enhancing the UV-Vis spectra ralated to the photocatalytic decomposition of BPA.

3.3 Plausible Formation Mechanism of Nanocavities Inside Aligned 2D-TiO_2 Nanostructures

By accepting the Tauc plot we found that TiO_LYO_500, TiO_LYO_650, TiO_LYO_800, TiO_LYO_950 catalysts exhibited a band gap energy higher than that of the P25 catalyst [54] (Figure 9), and thus these catalysts can absorb in the UV light region. The conduction band electrons (e^-) and valence band holes (h^+) are generated when an aqueous suspension of 2D TiO_2 nanosheet shaped catalysts is irradiated by UV light (λ_{max} = 365 nm). Banerjee et al. [71] calculated the effect of nanocavities formed in Si thin films on the effective optical absorption coefficient. Theyobserved a significant enhancement of the molar absorption koeficient (ε) by introducing nanocavities and this was due to the back-scattered light (Rayleigh scattering for small nanocavities, and the gradual transition from Rayleigh scattering to diffraction phenomena in the case of large nanocavities) effects from the nanocavities. This model can also be used to explain the abnormal optical absorption behaviour of the as-prepared 2D TiO_2 nanosheets samples, especially these of the TiO_LYO_800 material. In the high-wavelength region (λ ~ 365 nm), the effect of back-

scattered light from the nanocavities is not obvious as the size of nanocavities is far less than the wavelength of the light. The effective 2D TiO_2 nanosheet thickness could play a crucial role, since the calculated ε of the TiO_2 nanorods with the nanocavities might be less than the effective ε. However, at a lower wavelength range (λ > 365 nm) the size of the nanocavities is close to λ, so the effect of back-scattered light from the nanocavities can become significant and therefore makes the ε of the 2D TiO_2 nanosheets with nanocavities higher than that without nanocavities [52]. These results are consistent with Banerjee and Han [24,71] theoretical model for ε and support the assumption that creating deep "nanopockets" in TiO_2 photocatalysts may be a method to modify the density of active sites and can provide extra accessibility to different organic pollutants adsorbed on their surface. Once the water and ammonium molecules depart from the 2D TiO_2 nanosheets, and crystals are adopted by empty spaces, the TiO_2 structure begins to change when the temperature rises from 650 to 950 °C. The heating process does change the morphology of nanocavities, which appear as merged hexagons and rectangles in case of anatase (TiO_LYO_800) and hexagons in the case of rutile crystals (TiO_LYO_950). Therefore, it can be assumed that the morphology of the nanocavities is influenced by the anatase-rutile polymorph TiO_2 evolution competing reactions during the annealing procedure.

4. Conclusions

In this work, a freeze-drying strategy is developed by employng PPTA as a precursor to prepare ultrathin 2D TiO_2 nanosheets. We investigated the dynamics of water nanoconfined in as-prepared ultrathin 2D titania nanosheets. The proposed freeze-drying strategy opens up a promising avenue for designing 2D nanostructures for versatile materials, with intrinsically layered structures, for broad applications in nanoscience, nanotechnology and environmental monitoring. Heat treatment from 500 to 950 °C of the pristine lyophilized material does not lead to scolling of the 2D TiO_2 nanosheets and no altering of the structure of anatase crystallites occurs. The annnealing process causes the evaporation of nanoconfined water which leaves empty spaces inside the 2D TiO_2 nanosheets and eventually become self-assembled nanocavities ("nanopockets") along certain crystallographic directions of anatase and/or rutile nanocrystals. The nanocavities with size ranging from 5 to 10 nm in both, length and width, and depth of about 3.6 nm are responsible for the enhacement of the optical absorption and the photocatalytic degradation of BPA under UV irradiation.

Acknowledgments

This research is supported by the Czech Science Foundation (project No.18- 15613S). The authors gratefully acknowledge Prof. Robert F. Klie from the UIC Chicago for his helpful and instructive discussion focused on nanocavities phenomenon, Jakub Mares for technical assistance and both reviewers for their very constructive recommendations.

Appendix A. Supplementary data

The following is Supplementary data to this article:

References

[1] J. N. Coleman, M. Lotya, A O'Neill, Sh.D.Bergin,P.J. King , U. Khan, K. Young, A. Gaucher, S. De, R. J. Smith, I. V. Shvets, S.K. Arora, G. Stanton, H.Y.Kim, K. Lee, G. T. Kim, G.S. Duesberg, T. Hallam, J.J. Boland, J.J. Wang, Science 331 (2011) 568-571.
[2] M. Ferrer, F. del Monte, Chem. Mater. 20 (2008) 634-648.
[3] K.H. Rhodes, SA Davis, F. Caruso, B. Zhang, S. Mann. Chem. Mater. 12 (2001) 2832-2837.
[4] T. W. Kim, S. J. Hwang, S. H. Jhung, J. S. Chang, H. Park, W. Choi, J. H. Choy, Adv. Mater. 20 (2008) 539 – 542.
[5] T. W. Kim, S. G. Hur, S. J. Hwang, H. Park, W. Choi, J. H. Choy, Adv. Funct. Mater. 17 (2007) 307 – 314.
[6] M. Banerjee, S. K. Datta, H. Saha, Nanotechnology 16 *(*2005) 1542-1545.
[7] D. Majumdar, S. Chatterjee, M. Dhar, S. K. Dutta, H. Saha, Sol. Energy Mater. Sol. Cells 77 (2003) 51-56.
[8] P. D. Yang, D. Zhao, D. Y. Margolese, B. F. Chmelka, G. D.Stucky, Nature 396 (1998) 152-155.
[9] R. L. Putnam, N. Nakagawa, K. M. McGrath, N. Yao, I. Aksay, S. M. Gruner, A. Navrotsky, Chem. Mater. 9 (1997) 2690-2697.
[10] J. H. Evans, Nature 229 *(*1971) 403-407.
[11] G. Muller, R. Brendel, Phys. Status Solidi A 182 (2000) 313-318.
[12] H. Seel, R. Brendel, Thin Solid Films 608 (2004) 451–452.
[13] R.A. Caruso, M. Antonietti, Adv. Funct. Mater.12 *(*2002) 307-312.
[14] A. Bigi, E. Boanini, D. Walsh, S. Mann, Angew. Chem., Int. Ed. 41 (2002) 2163-2166.
[15] J.J. Spivey, Handbook of Heterogeneous Catalysis (2nd Edition) 5 (2008) 2394-2411.
[16] I.S. Cho, M. Logar,C.H. Lee, L. Cai, F.B. Prinz, X. Zheng, Nano Lett. 14 (2014) 24-30.
[17] R.Daghrir, P.Drogui, D.Robert, Ind. Eng. Chem. Res.52 (2013) 3581– 3599
[18] J.M Herrmann, Catal. Today, 35 (1999) 115–129.
[19] A Linsebigler, G. Lu, J.T .Yates, Chem. Rev., 95 (1995) 735–750.
[20] Y. J Hwang, C .Hahn, B Liu, P .Yang, ACS Nano 6 (2012) 5060–5069.
[21] N.Liu, C . Schneider, D. Freitag, M. Hartmann,U. Venkatesan, J. Müller,E. Spiecker, P. Schmuki, Nano Lett.14 (2014) 3309–3313.
[22] Y C. Pu,Y. Ling, K. D Chang, C. M Liu, J. Z . Y. J Zhang, Y. Hsu, J. Phys. Chem. C, 118 (2014) 15086–15094.
[23] Fu Ning, Wu Yuqi, Jin Zhiliang, Lu Gongxuan, Langmuir 26 (2010) 447–455.
[24] W.Q Han, L. Wu, R. F. Klie, Y. Zhu, Adv. Mater. 19 (2007) 2525–2529.
[25] S. Usseglio, A. Damin, D. Scarano, S. Bordiga, A. Zecchina, C. Lamberti, J. Am. Chem. Soc., 129 (2007) 2822-2828.
[26] Z. H Zhang, P Wang, Energy Environ. Sci., 5 (2012) 6506–6511.

[27] K Pan, Y Dong, W Zhou, Q Pan, Y Xie, T Xie, G Tian, G Wang, ACS Appl. Mater. Interfaces 5 (2013) 8314–8320.
[28] Z. Xing, W. Zhou, F. Du, L. Zhang, Zh. Li, H. Zhang, W. Li, ACS Appl. Mater. Interfaces 6 (2014) 16653−16660.
[29] E. Plizingrova , L. Vilfova, P. Svora, N. Labhsetwar, M. Klementova, L. Szatmary, J. Subrt, Catalysis Today 240 (2015) 107-113.
[30] E. Greiner, T. Kaelin, K. Nakamura, CEH Report by SRI Consulting, Reversibility of chronic disease and hypersensitivity, 4 (2018), Taylor and Francis Group, LLC.
[31] CD LaPlante, MC Catanese, R. Bansal, LN Vandenberg**,** Endocrinology. 158 (2017) 3448-3461.
[32] S. Flint, T. Markle, S. Thompson, E. Wallace, J. Environ Manage 104 (2012) 19-34.
[33] R. Loos, R. Carvalho, D.C. António, S. Comero, G. Locoro, S. Tavazzi, B. Paracchini, M. Ghiani, T. Lettieri, L. Blaha, B. Jarosova, S. Voorspoels, K. Servaes, P. Haglund, J. Fick, R.H. Lindberg, D. Schwesig, B.M. Gawlik, Water Res. 47 (2013) 6475-6487.
[34] J. Tijani, O. Fatoba, L.F. Petrik, Water, Air, Soil Pollut. 224 (2013) 1-29.
[35] X. Zhang,' J. Yuan,' Yi Yu'Q. Dong,' Z. Xiong,'H. Yu, X. Zhu, H. Shen, Y. Xie, J. Alloys Compounds, 712 (2017), 549-554.
[36] S. Bakardjieva, J. Subrt, P. Pulisova, M. Marikova, L. Szatmary, Mater. Res. Soc. Symp. Proc. 1352 (2011) Materials Research Society. http://doi: 10.1557/opl.2011.1132.
[37] JCPDS PDF-4 database, International Centre for Diffraction Data, Newtown Square, PA, USA, release 2015
[38] P. Scherrer, Nachr Ges Wiss Goettingen, Math-Phys Kl. 1918 (1918) 98-100.
[39] J.L. Labar, Ultramicroscopy, 103 (2005) 237-249.
[40] S. Brunauer, P.H. Emmett, E. Teller, JACSS 60 (1938) 309-319.
[41] E.P. Barrett, L.G. Joyner, P.P. Halenda, JACS 73 (1951) 373-380.
[42] SasView version 4.1.2 software, http://doi: 10.5281/zenodo.825675.
[43] P.W. Schmidt, J. Appl. Cryst., 24 (1991) 414-435.
[44] K. Chiang, T.M. Lim, L. Tsen, C.C. Lee, Appl Catalysis A: General, 261 (2004) 225-237.
[45] SL Murov, I Carmichael, GL Hug, Handbook of Photochemistry, 2nd edn. CRC Press (1993)
[46] K. Davididou, E. Hale, N. Lane, E. Chatzisymeon, A. Pichavant, J.F. Hochepied, Catalysis Today 287 (2017) 3 – 9.
[47] J.Peral. D. Ollis, J of Catalysis 136 (1992) 554-565.
[48] H. Al-Ekabi, N. Serpone, Langmuir 5 (1989) 250-255.
[49] J. Theurich, M. Lindner, D. W. Bahnemann, A Kinetic and Mechanistic Study. 12 (1996) 6368–6376.
[50] G. Colón, M.C.Hidalgo, J.A. Navío, Appl. Catal. A, 23 (2002) 185-189.
[51] E. Plizingrova, M. Klementova, P. Bezdicka, J. Bohacek, Z. Barbierikova, D.Dvoranova, M. Mazur, J. Krysa, J. Subrt ,V. Brezova, Catalysis Today 281 (2017) 165-180.
[52] S. Bakardjieva, J. Subrt, V. Stengl, MJ Dianez, MJ Sayagues, Appl Catal.B: Environmental 58 (2005) 193-202.
[53] P. Pulisova, E. Vecernıkova, M. Marıkova, V. Balek J. Bohacek J. Subrt , J Therm Anal Calorim 108 (2012) 489–492.
[54] E. García-González, M. D. Soriano, E. Urones-Garrote and J. M. López Nieto, Dalton Trans., 43 (2014) 14644–14652.
[55] I. M. Szilagyi, J. Madarasz, G. Pokol, P. Kiraly, G. Tarkanyi, S. Saukko, J. Mizsei, A. L. Toth, A. Szabo and K. Varga-Josepovitso, Chem. Mater., 20 (2008) 4116-4120.
[56] J. Subrt, P. Pulisova , J. Bohacek, P. Bezdicka, E. Plizingrova, L. Volfova, J. Kupcık, Mat. Res. Bull., 49 (2014) 405–412.
[57] L.B. McCusker, F.Liebau, G. Engelhard, Pure and Appl Chem. 73 (2009) 381–394.
[58] E.Y. Kim, D.S. Kim, B.T. Ahn, Bull. Korean Chem. Soc. 30 (20019) 193-196.
[59] T. Kasuga, M. Hiramatsu, A. Hoson, T. Sekino, K. Niihara, Langmuir 14 (1998) 3160-1368.

[60] J. Subrt, P. Pulisova, J. Bohacek, P. Bezdicka, E. Plizingrova, L. Volfova, J. Kupcik, Mater. Res. Bull., 49 (2014) 405-412.
[61] S.J. Gregg, K.S.W. Sing, Adsorption, Surface Area and Porosity, 2nd ed.; Academic Press: London, 1991
[62] Z. Bo, C. George, J.R. Gallagher, J.T. Miller, P.C.Stair, J. M. Notestein, In Nanoscale Science and Engineering Forum Core Progr Area at the 2014 AIChE Annual Meeting (282).
[63] eBook, Small Angle Scattering from confined and interfacial fluids, Y. Melnichenko, http://doi10.1007/978-3-319-01104-2
[64] SASfit: software, I. Breßler, J. Kohlbrecher, A. F. Thünemann, J. Appl. Cryst. 48 (2015) 1587-1598.
[65] N. Rajeswari, A. Yogamalar, Ch. Bose, Appl Phys A 103 (2011) 33–42.
[66] B. Bharti, S. Kumar, HNo Lee, R. Kumar, Scientific Reps. 6, (2016).Article No.32355.
[67]. RN Aljawf, MJ Alam, F. Rahman, S. Ahmad, A. Shahee, S. Kumar, Arabian J of Chemistry, 2018, https://doi.org/10.1016/j.arabjc.2018.04.006
[68] G Li, J. Boerio-Goates, B F Woodfield, L. Li, Appl. Phys. Lett. 85 (2004) 2059–2061.
[69] G Li, L. Li, J. Boerio-Goates, BF Woodfield, J. Am. Chem. Soc. 127 (2005) 8659–8666.
[70] V. Swamy, D. Menzies, BC Muddle, A. Kuznetsov, LS Dubrovinsky, Q. Dai, V. Dmitriev, Appl. Phys. Lett. 88 (2006) Art. No 243103.
[71] M. Banerjee, S.K. Datta, H. Saha, Nanotechnology 16 (2005) 1542-1548.